Bulletin of the Seismological Society of America, Vol. 99, No. 5, pp. 2662–2680, October 2009, doi: 10.1785/0120080302

Anomalous Seismic Attenuation along the Plate Collision Boundary in Southeastern Taiwan: Observations from a Linear Seismic Array

by Chien-Ping Lee,* Naoshi Hirata, Bor-Shouh Huang, Win-Gee Huang, and Yi-Ben Tsai

Abstract Lateral variations of seismic attenuation are investigated using data from a linear seismic array deployed across southern Taiwan. The attenuation parameter t^* is obtained by fitting the amplitude spectra of P and S waves with a theoretical spectrum using an ω^2 model. The observed t^* data are then plotted against the travel time, back azimuth, and focal depth, respectively, to explore the spatial variations of t^* for P and S waves. Significant lateral variations of seismic attenuation are found between the eastern mountainous and western plain areas of Taiwan. Large attenuation contrast with depth in the east indicates that an anomalously high-attenuation zone is located in a shallower area north of the array in southeastern Taiwan. A 2D raytracing method is applied to show that the probable depth of the anomalous zone is at about 15–20 km. This anomalous attenuation zone coincides with an area marked by low-P and low-S velocities as well as a total absence of seismicity. The area is also marked by other prominent manifestations of active collision between the Eurasian and Philippine Sea plates, for example, high mountain ranges, rapid uplift, and high heat flows.

Introduction

Taiwan is located in the boundary between the Eurasian and Philippine Sea plates. The Eurasian plate subducts under the Philippine Sea plate in southern Taiwan whereas the Philippine Sea plate subducts under the Eurasian plate in northeastern Taiwan. Between these two subduction zones the two plates converge along the northwest–southeast direction at about 80 mm/yr. The collision between the two plates is most intense in southeastern Taiwan where the tallest peaks of the Central Ranges stand. Frequent earthquakes are common near the east coast of Taiwan along the boundary of the two colliding plates (Fig. 1). Curiously, a remarkable aseismic area beneath the southeastern Central Range can be seen from the seismicity map. Although previous studies indicate that the aseismic area may be associated with geothermal and/or partial melt effects (Ma *et al.*, 1996), its cause remains a puzzle.

Seismic attenuation is a physical parameter representing anelastic behaviors of materials along which seismic waves propagate. Because attenuation of seismic waves is also very sensitive to temperature, cracks, and fluid content in the material, study of seismic attenuation may provide clues about its physical state. On a small laboratory scale, seismic attenuation can be measured directly from a sample (Jones and Nur, 1983). On an intermediate scale from several meters to hundreds of meters, anelastic behaviors can be studied as deamplification effects of local site response by both geotechnical engineers and seismologists (Lee *et al.*, 2006).

On a large scale from several kilometers to hundreds of kilometers, seismic attenuation of tectonic structures can be studied by the analysis of seismic waves. Attenuation structures related to fault zones, collision belts, and subduction zones have been successfully studied by using local or regional earthquake sources (e.g., Scherbaum, 1990; Lees and Lindley, 1994; Sarker and Abers, 1998; Eberhart-Phillips and Chadwick, 2002). This study will focus on seismic attenuation along the plate collision boundary in southeastern Taiwan aiming to shed new light on the possible cause of an aseismic zone there.

Seismic attenuation of P waves and S waves in Taiwan has been studied previously using data from the Telemetered Taiwan Seismographic Network (TTSN) and the Central Weather Bureau Seismic Network (CWBSN) (e.g., Chen *et al.*, 1996; Chen, 1998). The available station numbers of the TTSN and the CWBSN for these studies, about 25 and 45, respectively, were not sufficient to resolve detailed spatial seismic attenuation structures in the whole of

*Also at: Earthquake Research Institute, University of Tokyo, Tokyo, Japan.

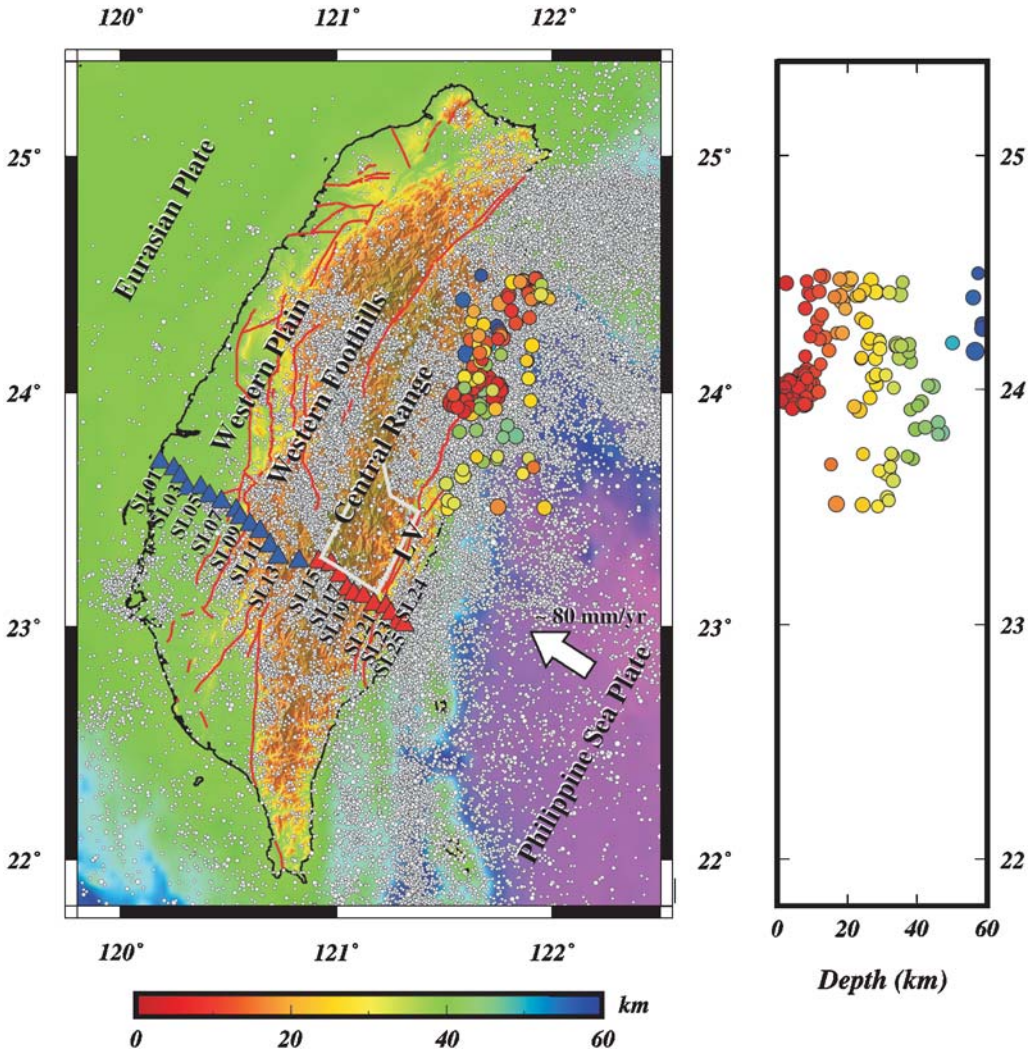

Figure 1. Locations of the seismic array and source events used in this study. The background shows the topography and bathometry of Taiwan. LV denotes the Longitudinal Valley. The red lines show active faults. The station codes of the array are SL01–SL25 from west to east, respectively. The blue triangles show the 14 western stations (SL01–SL14) and the red triangles show the 11 eastern stations (SL15–SL25) on an east–west linear seismic array deployed across southern Taiwan. Color circles show the 153 events whose seismic data are used in this study. The color bar in the bottom shows the scale of the focal depth of these events. Background seismicity shows $M > 3$ earthquakes (1900–2003) from the catalog of the TCWB. The gray frame denotes the aseismic area. The right-hand panel shows the depth distribution of the selected events along a north–south profile.

Taiwan. Besides, both TTSN and CWBSN are short-period seismic networks providing data with a limited frequency bandwidth.

These limitations are overcome by the recent deployment of many broadband seismic instruments in Taiwan. High-quality seismic data obtained by these new seismic instruments can be used to study detailed regional attenuation structures. In particular, a linear broadband seismic array with small spacing was deployed across southern Taiwan. High-quality seismic data from this array were used in this study to explore detailed attenuation structures in southern Taiwan. We analyzed spatial variations of attenuation parameters to identify potential anomalous attenuation zones across southern Taiwan. As a result we have found a zone of high attenuation for both *P* and *S* waves that is probably associated with the aseismic zone beneath southeastern Taiwan.

Data and Method

In order to understand crustal structures and geodynamic processes of recent orogeny in Taiwan, a linear seismic array consisting of 25 broadband stations, at nearly even spacings of 4–5 km, was deployed across southern Taiwan in April 2005, as shown in Figure 1, by the Institute of Earth Sciences, Academia Sinica (Huang *et al.*, 2006). Each station consists of a three-component broadband seismometer, a 24 bit analog-to-digital converter, a large memory capacity digital recorder, and a Global Positioning System (GPS) receiver. Output signals from each seismometer are

continuously recorded at a 100 Hz sample rate. The waveform data are excellent for spectral analysis.

Records from 153 earthquakes located at a latitude between 23.4° and 24.5° and a longitude between 121.5° and 122.0° from April 2005 to July 2006 are selected to provide sufficient coverage of ray paths across the aseismic zone (Fig. 1). Only events with M_L magnitude greater than 3.5 are selected to ensure well-recorded waveforms at all stations. The ranges of earthquake magnitude for all events are between 3.5 and 5.0 except four events that are between 5.0 and 5.5.

A total of 3213 *P*- and 3421 *S*-wave arrivals are manually picked from the seismograms. Signals on the two horizontal components are rotated to longitudinal and transverse components before picking the *S*-wave arrivals. *P*- and *S*-wave arrivals are picked from the vertical and transverse components of seismograms, respectively. After removal of instrumental response the velocity waveforms are further integrated to yield corresponding displacement waveforms (Fig. 2). We then obtain the amplitude spectra of tapered *P* and *S* displacement waveforms by using fast Fourier transform (FFT). For this, a 5 sec time window (starting 1 sec before the *P* arrival time) for *P* waves and a 10 sec time window (starting 2 sec before the *S* arrival time) for *S* waves are adopted, noting that sufficiently long time windows are needed for stable estimation of t^* (Lees and Lindley, 1994). Furthermore, 10% and 20% Hanning tapers are applied, respectively, which is 0.5 sec for a *P* wave and 2 sec for an *S* wave at both ends of the time windows before FFT.

An observed earthquake spectrum is the combination of source, path, site, and instrument effects. It can be represented as

$$H(f) = S(f)P(f)R(f)I(f), \tag{1}$$

where $H(f)$ is the observed spectrum, $S(f)$ the source spectrum, $P(f)$ the path spectrum, $R(f)$ the site spectrum, and $I(f)$ the instrument response. The instrumental response $I(f)$ is removed at the beginning, as mentioned previously. The path effect, together with other contributions, can be quantified through model fitting of the observed spectrum. The theoretical displacement spectra of the source, path, and site can be written separately as

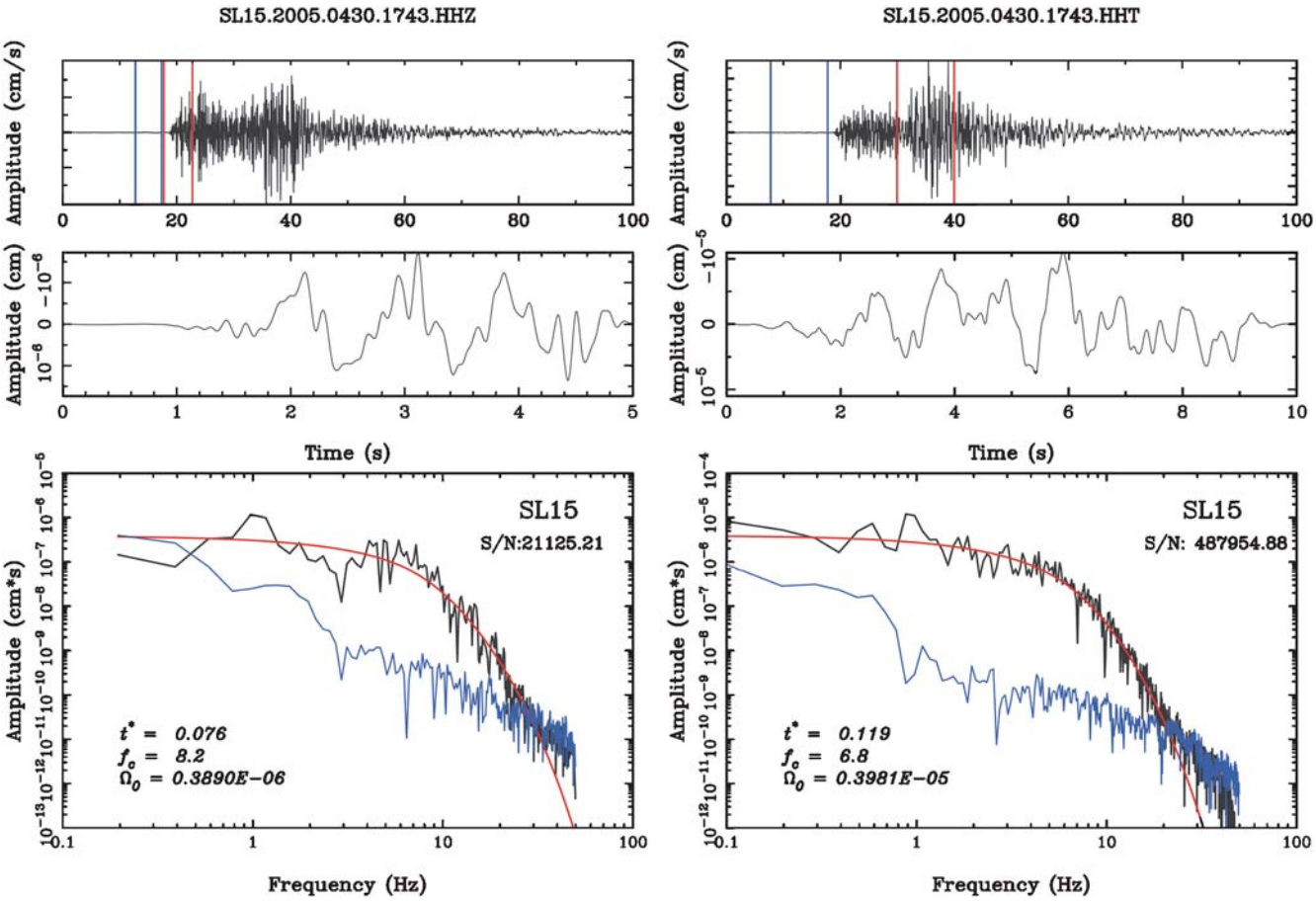

Figure 2. Examples of seismograms for *P* and *S* waves, in the left- and right-hand columns, respectively, in the time and frequency domains. In each column, the top frame shows the velocity waveform starting from the origin time. The vertical lines show the signal (red) and noise (blue) windows. The middle frame shows the integrated displacement waveform for the signal window after removal of instrumental response. The bottom frame shows the observed noise spectrum (blue), the observed signal spectrum (black), and the best-fitting theoretical spectrum (red) obtained by adjusting the t^*, f_c, and Ω_0 parameters.

$$S(f) = \frac{\Omega_0}{[1 + (f/f_c)^{2\gamma}]^{1/2}} \tag{2}$$

and

$$P(f)R(f) = \exp(-\pi t^* f), \tag{3}$$

where f is the frequency, Ω_0 the low-frequency spectral asymptote, f_c the corner frequency, γ the source spectral fall-off, and $t^* = t_i^* f^{-\alpha}$, where t_i^* and α are attenuation parameters (Lindley and Archuleta, 1992; Lees and Lindley, 1994). An ω^2 model for the source spectrum (Aki, 1967; Brune, 1970, 1971) is used here as a reference to determine t^* from observations. In this study attenuation is assumed to be independent of the frequency in order to simplify the parameters (i.e., $\alpha = 0$) (Lees and Lindley, 1994). When t^* is independent of frequency, it becomes identical to κ (Anderson and Hough, 1984; Hough *et al.*, 1988). κ is an empirical spectral decay parameter that indicates the attenuation characteristics of observed spectra. The remaining parameters, t^*, f_c, and Ω_0, are obtained by fitting the observed spectrum with the theoretical spectrum using an ω^2 source model (i.e., $\gamma = 2$) (Aki, 1967; Brune, 1970).

A grid search method is applied to determine these parameters by matching the observed and theoretical spectra over a frequency range from 1 to 20 Hz. The high-frequency cutoff is set at 20 Hz to minimize the effect of noise. We do not constrain f_c in this study, because previous studies have shown that the difference between constrained and unconstrained f_c is not significant (Sarker and Abers, 1998).

In order to obtain reliable estimates of the attenuation parameters, a strict criterion of a signal-to-noise (S/N) ratio > 100 is adopted for additional data screening (Fig. 2). The S/N ratio is calculated from the amplitudes of the signal window and a preevent window in the frequency domain. For P waves, the noise amplitude is determined from each seismogram over a 5 sec time window immediately preceding the signal window of P-wave arrival. For S waves, the noise amplitude is determined from each seismogram over a 10 sec time window prior to the signal window of P-wave arrival. Finally, a total of 1429 t^* values for P waves and 2936 t^* values for S waves are included for this study.

The site effect on attenuation is combined with the path effect in t^*, as shown in equation (3). In order to separate the path and site effects, a path-averaged attenuation equation is introduced:

$$\begin{aligned} t^*(P,S) &= \int_{\text{ray path}} \frac{1}{Q_{(P,S)} V_{(P,S)}}\, dr = t_0^*(P,S) + \frac{R}{\bar{Q}\overline{V}} \\ &= t_0^*(P,S) + \frac{T_{(P,S)}}{\bar{Q}_{(P,S)}}, \end{aligned} \tag{4}$$

where $t^*(P,S)$ is the observed attenuation parameter defined for either P or S waves, $t_0^*(P,S)$ represents the near-station site effect of t^*, $Q_{(P,S)}$ is the quality factor for P or S waves, and $V_{(P,S)}$ is the P- or S-wave velocity along the ray path. The integral is taken along the ray path for $V_{(P,S)}$. R is the distance of ray paths for a P or S wave. $\overline{V}$ represents the path-averaged velocity of relevant phases. T is the travel time for a P or S wave. The slope ($\bar{Q}^{-1}$) shows the path-averaged attenuation in the right term of the equation.

Because the geometrical constraints due to the layout of the linear seismic array and earthquake source distribution are not optimal for tomography, we will analyze the spatial variations of t^* at each station to demonstrate lateral and vertical variations of attenuation structures instead of attenuation tomography. This will allow us to obtain attenuation structures from t^*, yet avoid the resolution problem in the tomography method due to geometrical constraints. Furthermore, it is not necessary to know the velocity model before obtaining seismic attenuation when P- and S-wave travel times are used in equation (4). In this way we can plot the attenuation parameter t^* as a function of travel time.

Results

As a seismic wave travels from a source to a station it carries information about the subsurface structure through which the seismic wave passes. A seismic ray is often defined by three spatial parameters, that is, travel time, back azimuth, and incident angle of the ray. In a map view of seismic rays, the travel time reflects the distance between the event and the station as well as the velocity characteristics of the ray path. The back azimuth prescribes the direction of an incoming ray at a station that is measured clockwise from the north. These two parameters can be used to resolve the spatial variations of t^* in map view, revealing locations of anomalous t^*. For variations of t^* with depth, the depth of ray paths is a key parameter that depends on the incident angle. Because, in addition to the incident angle a velocity model is needed to obtain the depth of ray path, we will not use the incident angle in this study.

Equation (4) defines a positive linear relationship between t^* and travel time if the attenuation structure is assumed to be uniform. The linear trend of t^* will be perturbed if there are attenuation variations along the ray paths. Figure 3 shows an example of rays passing through an anomalous zone at one of the stations (SL24). The data points in the parallelogram show clustering along a linear trend, revealing a distance dependence of t^* perturbed by significant lateral and vertical variations of attenuation structure from different ray paths. In the meantime, a group of high-t^* data in the oval circle above the linear trend indicates that some group of ray paths has passed through an anomalous zone of high attenuation. In this case it is not appropriate to obtain an average attenuation ($\bar{Q}^{-1}$) from all t^* data at station SL24 by equation (4) because the ray paths include a group of high-t^* data from the anomalous zone that will bias the linear trend. Instead, we choose to look at the trends of t^* in shorter 5 sec intervals of travel time to highlight the variations of t^* with travel time. Figure 4a shows the relationship between

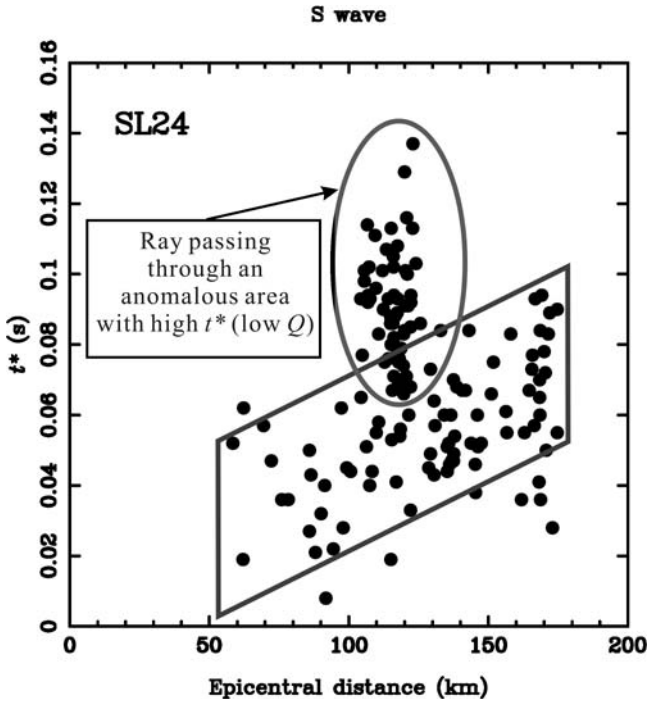

Figure 3. Plot of the observed t^* versus epicentral distance at station SL24. The parallelogram shows a linear trend of t^* that is proportional to the epicentral distance. The oval shows anomalous t^* values from rays passing through an anomalous attenuation zone.

t^* and travel time for S waves at each station that generally shows a linear trend similar to Figure 3. The colors of t^* in Figure 4 denote different travel times, which increase from blue to red. Large dispersions in t^* reveal the presence of complex attenuation structures. They also provide measures of perturbations in t^* estimation. The linear trend of t^* with travel time cannot be clearly seen at western stations SL01–SL06 because the travel times for all events are clustered in a short travel-time interval. In the figures we can find significantly higher t^* data at stations SL15–SL25 over some travel-time intervals for both individual t^* (dots) and the average t^* (black line).

Figure 4b shows fewer t^* data for P waves than S waves due to lower S/N ratios, especially for western stations (SL01–SL08) that are located in the densely populated alluvial plain areas (Fig. 1). Nevertheless, the t^* data for P waves still show similar patterns to the t^* data for S waves, although t^* values are generally smaller for P waves than S waves. It is noted that the levels of t^* are different among the stations for both P and S waves. This reflects different local characteristics of t^* near each station. For example, SL11, SL15, SL18, and SL22 show higher t^* than other stations. The intercept of the linear trend at each station, t_0^*, in equation (4) represents the local site effect on seismic attenuation at shallow layers that will be discussed later in this article.

Alternatively, we can look at the relationship between t^* and the back azimuth to explore lateral variations of t^* with the direction of incoming S waves, as shown in Figure 5a. The color codes of each t^* here are the same as those for Figure 4a. From the plot of t^* with back azimuth, we can see two peaks of t^* at some stations, as marked by red arrows for easy identification. Based on our inspection of the color codes for t^* in Figures 4 and 5 we can see that one of the peaks is due to large distance and the other due to an anomalous zone with high t^* in some particular back-azimuth directions. Theoretically, the t^* will increase with travel time according to equation (4), which shows the first peak due to large distances. The second peak is caused by anomalous variations of attenuation structure along ray paths. The two peaks of t^* move closer to each other for stations located further to the east along the linear array. This pattern of t^* variations with back azimuth suggests that the anomalous zone is not located near the stations, resulting from site effects of seismic attenuation, but is located in a specific structure along the ray paths. Similar patterns are also observed for P waves, as shown in Figure 5b, even though with fewer data.

The patterns of t^* variations with travel time and back azimuth, as shown in Figures 4 and 5, can be explained schematically in Figure 6. Figure 6a shows the features of average t^* versus travel time at the western (SL01–SL14) and eastern (SL15–SL25) stations for P and S waves as shown in Figure 4. The black line represents a theoretical linear trend of t^* with travel time, according to equation (4). The red line shows the trend of observed t^*. The peaks of observed t^* above the linear trend shift to longer travel time as stations move further toward the east.

Figure 6b can explain the patterns of high t^* for S and P waves, respectively, in Figures 5a and 5b due to changes in back azimuth. Equation (4) shows that a high t^* can result from a long ray path or a low-Q zone, or both. For a uniform structure, the long path will be the main factor of high t^*. However, Figure 5 shows that one peak of high t^* is most probably due to an anomalously low-Q zone present along the ray paths. Because an anomalous zone with high t^* implies the presence of a low-Q zone, we conclude that a low-Q zone exists in eastern Taiwan (Fig. 6b). Furthermore, by combining the patterns of t^* variations and raytracing based on the geometry of events and station, we find that the low-Q zone is most likely located along the ray paths not far to the north of the eastern stations.

In order to resolve the spatial variations of t^*, three tightly clustered groups are selected from the 153 events. Figure 7 shows the epicenters and depth distributions of the three groups. The northernmost group A consists of events clustered in a small area but their depth extends to a depth around 40 km. The middle group B consists of a dense shallow cluster of events in the upper 12 km and a few scattered, deeper events down to about 50 km. The southernmost group C consists of deeper events between 20 and 40 km. Figure 8a shows the t^* variations with travel time for S waves excluding data from the shallow cluster of group B. In contrast to Figure 4a, the data at each station show a clear linear trend without large kinks, especially for the eastern stations

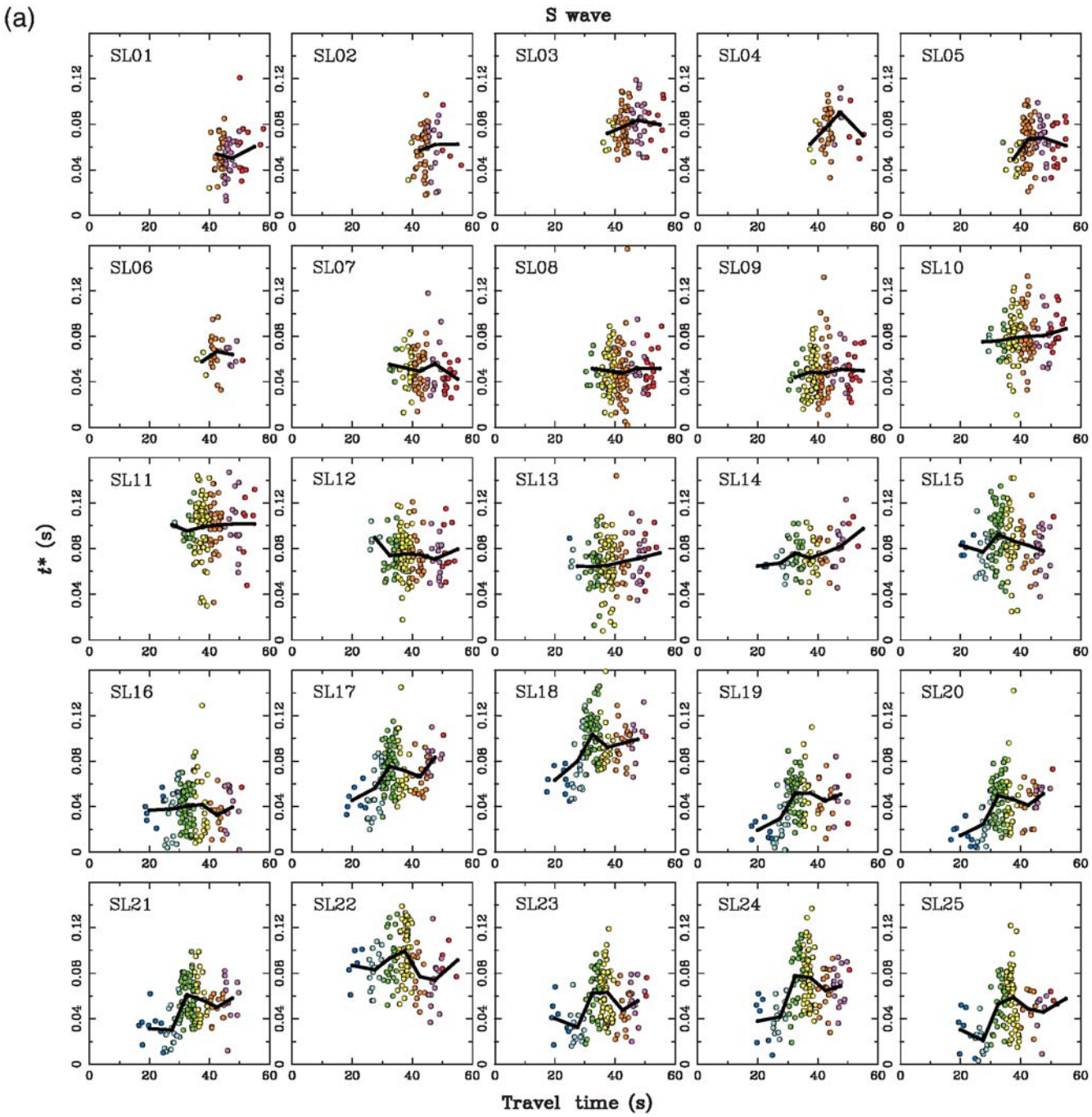

Figure 4. Plots of the observed t^* versus travel time at individual stations for (a) *S* waves and (b) *P* waves. The black line shows the average of t^* at 5 sec intervals. The colored dots denote increasing travel times from blue to red. (*Continued*)

(SL15–SL25). This linear trend of t^* with increasing travel time fits well with equation (4).

Figure 8a shows that the slopes of the average t^* (black line) are flatter at the western stations but steeper at the eastern stations. This suggests that the average seismic attenuation along the ray paths is higher toward the eastern stations than that toward the western stations, even excluding the anomalous zone. From the slope of t^* versus travel time in Figure 8a, we obtain an average Q_S ($\bar{Q}_S$) of about 2000 for the western stations and only about 970 for the eastern stations. This clearly shows regional lateral variations in seismic attenuation between the eastern and western stations. The $\bar{Q}_S$ will be even lower at the eastern stations if data from ray paths traversing the anomalous zone are included. On the contrary, Figure 8b shows the data on t^* variations with travel time just for the shallow cluster of group B. By comparing Figure parts 8a and 8b, we find that, at the same travel time, the t^* values from the shallow cluster of group B

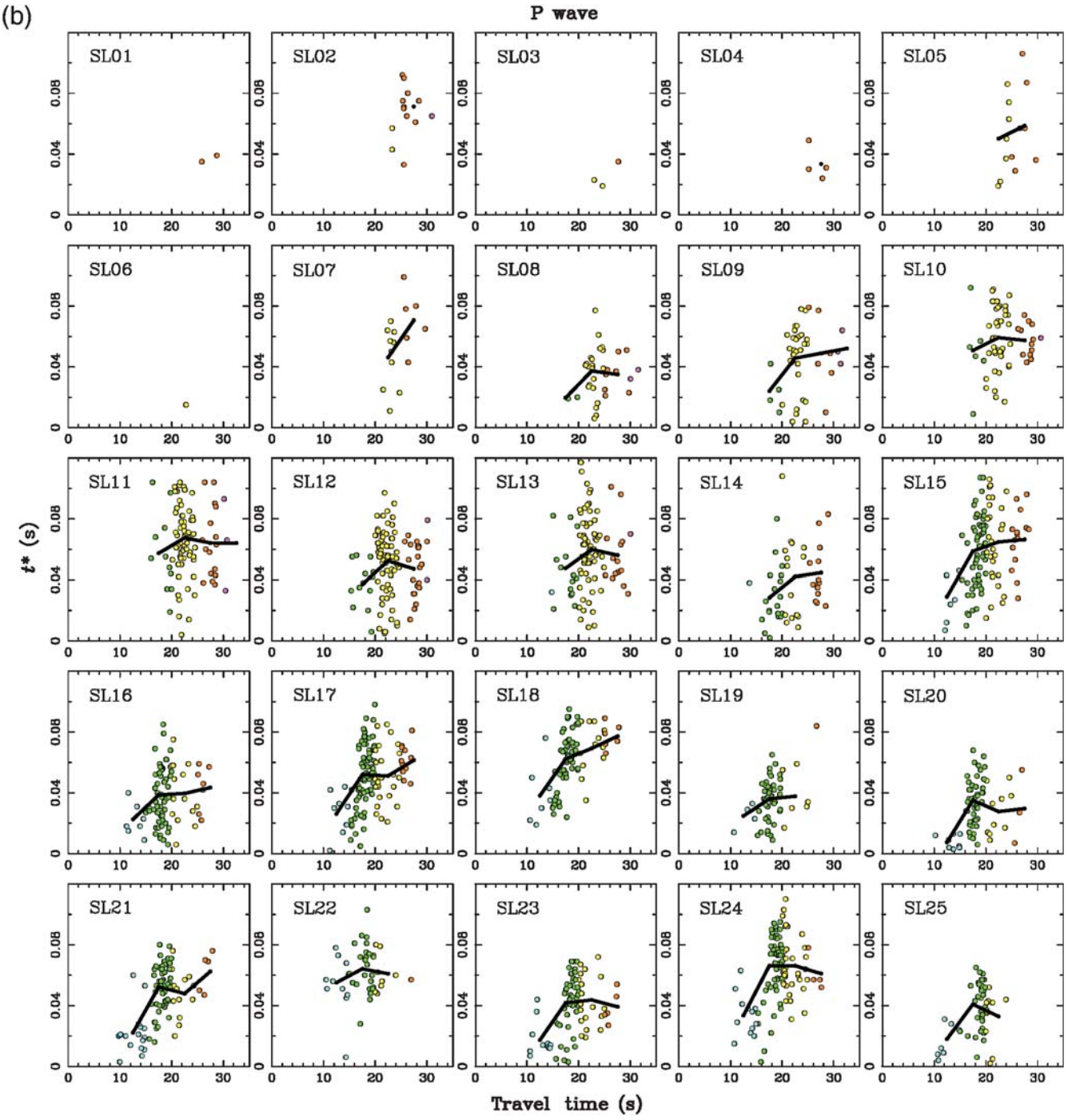

Figure 4. Continued.

are significantly higher than those from other events at the eastern stations. This means that the ray paths to the eastern stations from the shallow cluster of group B must have passed through an anomalous zone of high attenuation. Thus, a low-Q zone can be identified that lies along a region traversed by ray paths connecting the shallow group B events and the eastern stations, both in map view and in cross section. It is difficult to definitely estimate $\bar{Q}_S$ for the paths of the shallow cluster of group B due to limited travel-time ranges at eastern stations in Figure 8b. Still we can roughly estimate an average Q_S of about 630 for the paths of the shallow cluster of group B.

In order to resolve the spatial variations of t^* with depth, we present the data in another way. Figure 9a shows plots of t^* versus focal depth for S waves for the events shown in Figure 7. In general, there is a decreasing trend of t^* with increasing focal depth. In the figure we can also see that the slopes of t^* at the eastern stations (SL16–SL25) are

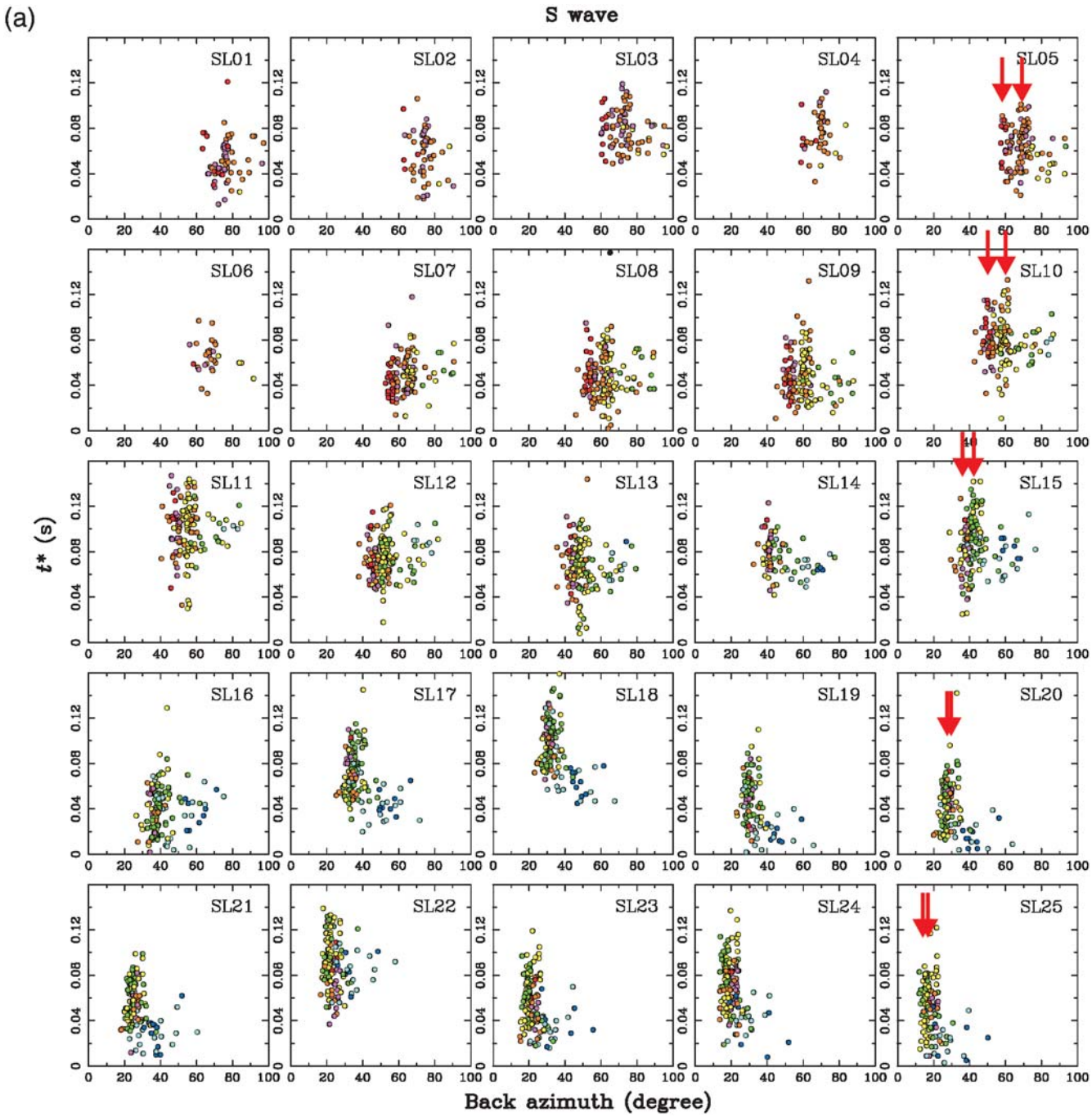

Figure 5. Plots of the observed t^* versus back azimuth at individual stations for (a) *S* waves and (b) *P* waves. The colored dots correspond to Figure 4. Red arrows indicate shifting of the high-t^* data toward more northerly directions as the station moves progressively toward east. (*Continued*)

significantly steeper than the western stations (SL01–SL15). This means that the variations of seismic attenuation with depth are greater for the eastern stations than the western stations. By comparing the t^* distributions from data of the three groups of events, we can find more detailed patterns of t^*. For the eastern stations (SL17–SL25) except SL22, the t^* of groups A, B, and C clearly ranks from high, medium, to low, successively, just like their variations with distance. Station SL22 shows a notably different pattern than the other eastern stations; it might be due to its location in the Longitudinal Valley, which marks the exact boundary of the Eurasian and Philippine Sea plates. Seismic waves traveling along it may be subject to scattering or focusing, thus affecting the results of t^* at station SL22. On the contrary, there is no clear ranking of t^* at western stations for the three groups of events.

From previous differences in the ranking of the three groups and the slope of t^* between the western and eastern

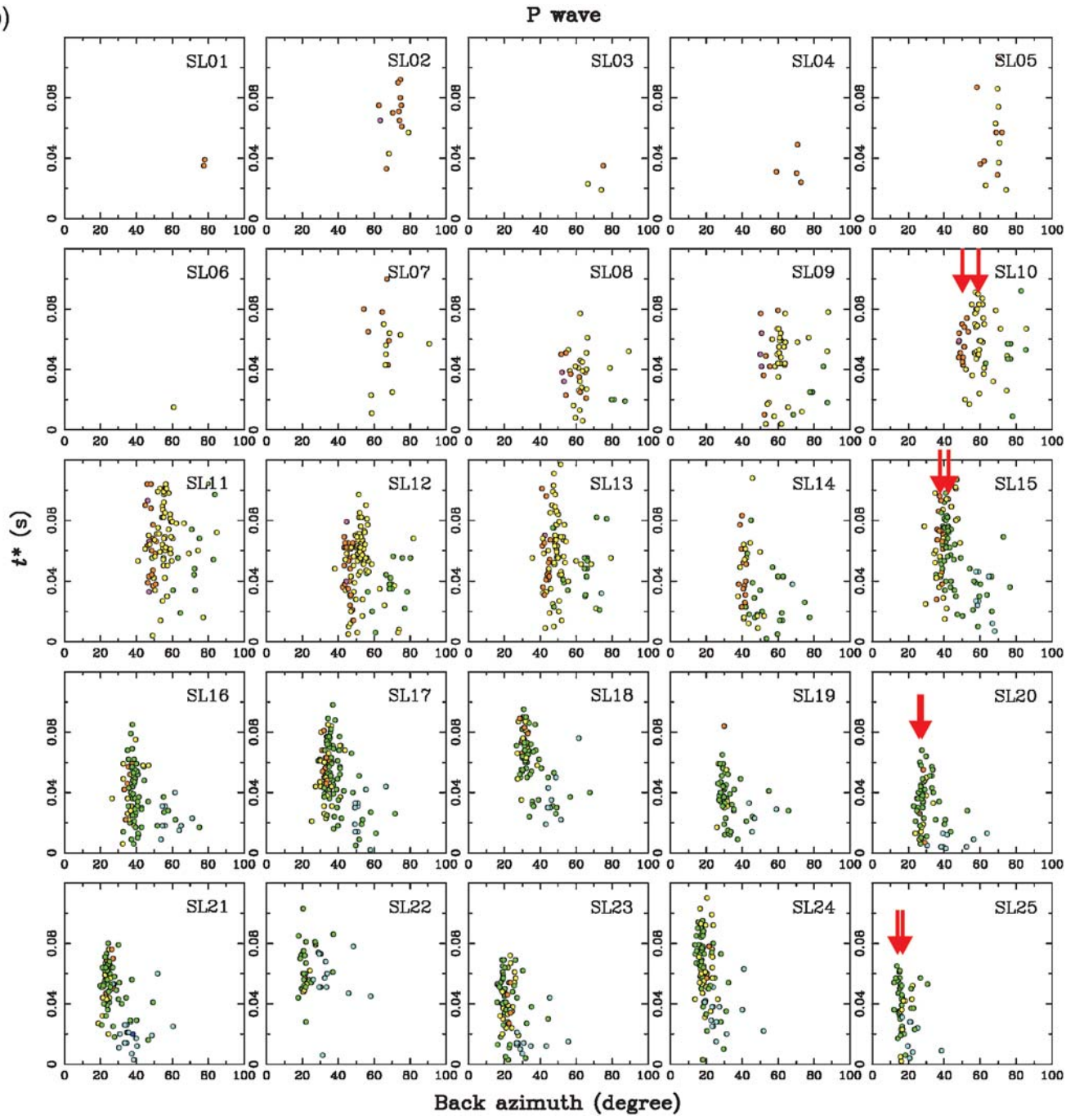

Figure 5. Continued.

stations in the plot of t^* with focal depth, two points can be inferred. First, equation (4) shows that t^* is proportional to hypocentral distance. Hypocentral distances from the three groups obviously differ more for the eastern stations than for the western stations. Therefore, the ranking of t^* among the three groups is more pronounced among the eastern stations. In addition, the ray paths from the shallow events (< 12 km) of group B yield the most anomalously high t^* at the eastern stations that will result in a steep slope in the plot of t^* with focal depth because high t^* corresponds to shallow focal depth. Second, there is no high t^* along the ray paths from group A but there are high t^* values along the ray paths from groups B and C at the western stations. Thus, the t^* values of the three groups are mixed together to give a gentle slope of t^* and focal depth at the western stations.

Following the previous inference, we find that the seismic attenuation contrast with depth is significant at the eastern stations. It also shows that a low-Q zone is located at the shallow part of the crust, north of the eastern stations. The anomalous zone apparently does not extend north of

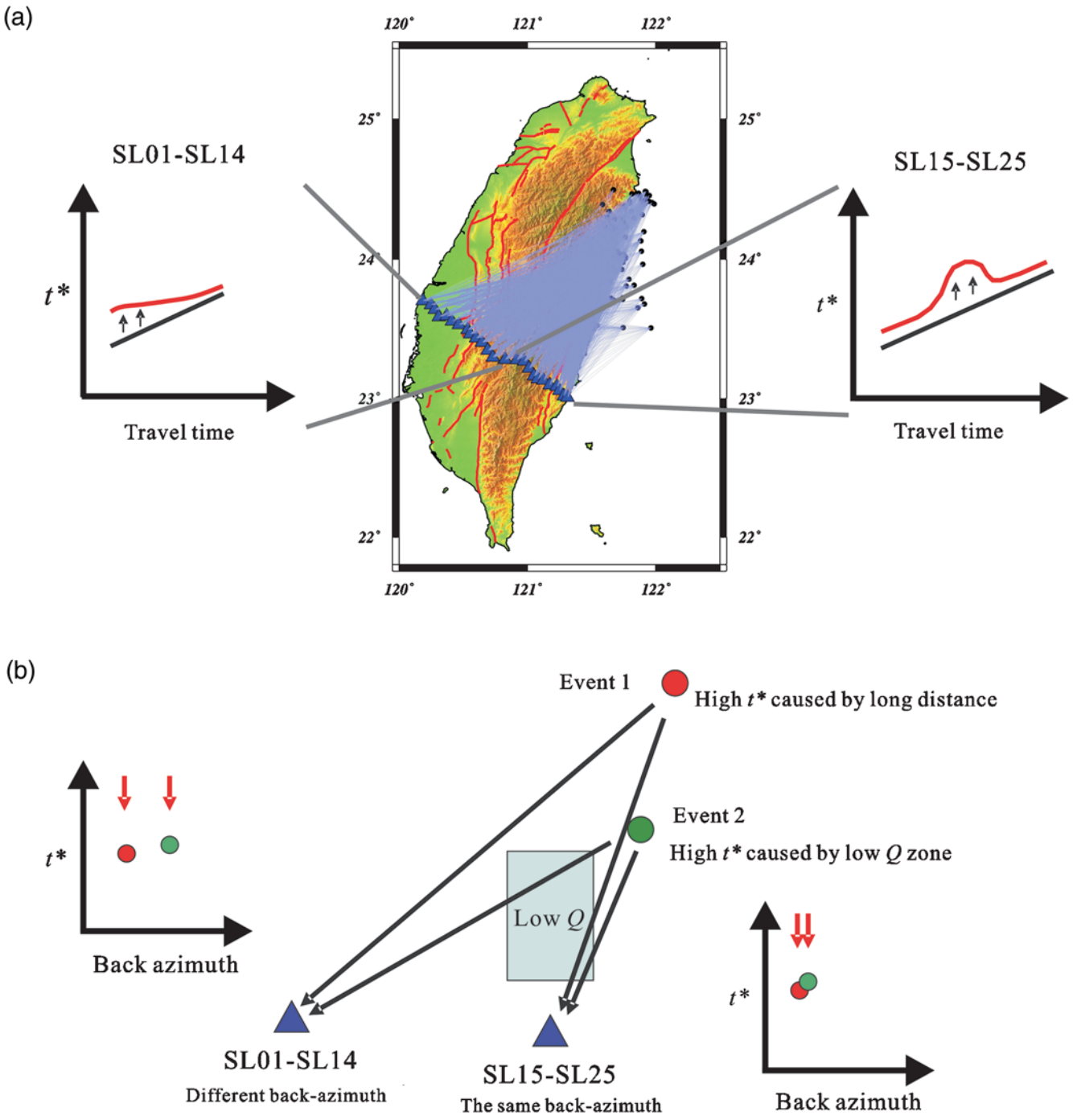

Figure 6. Schematic diagrams showing plots of t^* with a presumed low-Q zone as a function of (a) travel time and (b) back azimuth. (a) The peak of t^* (red line) above the linear trend (black line) shifts as the station moves toward the east. The black line denotes the theoretical line. The red line denotes the observed trend. (b) Long distance and a low-Q area can contribute to high t^*, respectively, for event 1 and event 2. Variations of the back azimuth separate the high t^* at stations SL01–SL14 (western stations) but move the high t^* together at stations SL15–25 (eastern stations) when a low-Q area is present. Red arrows indicate the peaks of t^*.

group B because we do not find a similar feature of t^* for group A (Fig. 7). For P waves, roughly similar trends can also be observed at several stations as shown in Figure 9b. Figure 10 shows schematically the contrast of Q at depth between the western and eastern stations, which can explain the observed patterns of t^* in Figure 9. In the figure, the average Q_S values for the crustal attenuation structures are obtained from the slope in the plot of t^* with travel time, as shown in Figure 8.

The previous results suggest that we can identify an anomalous attenuation zone by using array data to show variations of t^* with travel time, back azimuth, and focal depth.

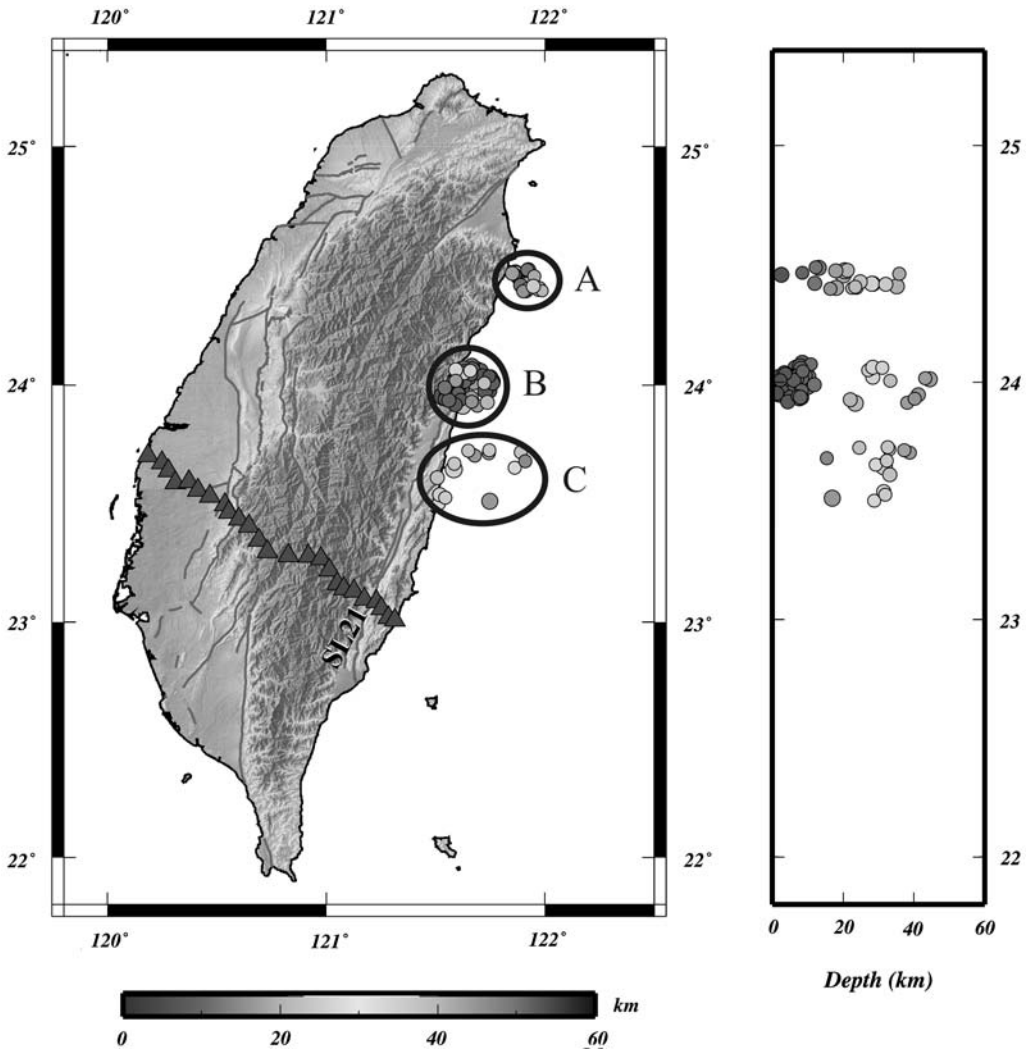

Figure 7. Three dense groups are selected from the 153 events. The triangles denote the seismic array. The lines show active faults. The gray bar shows the focal depth. The right-hand panel shows the depth distribution of events in a north–south profile.

The anomalous attenuation zone is present along the ray paths connecting group B events with the eastern stations, as shown by the shaded area in Figure 11. The area is located right on the boundary of the Philippine Sea and Eurasian plates that also coincides with the aseismic area, as shown in Figure 1.

The large contrast of seismic attenuation with depth under the eastern stations also points to a low-Q zone along shallow ray paths. Next, we would like to know the probable depth of the low-Q zone. A two-dimensional raytracing method (Zelt and Smith, 1992) is applied to determine the probable depth of the low-Q zone. A one-dimensional P-wave velocity model along the tectonic trend is adopted from Chen and Shin (1998). This velocity model is used for routine earthquake location by the Taiwan Central Weather Bureau (TCWB). Station SL21 is shown (Fig. 12) as an example.

Three groups of events are chosen to represent the locations of source, as shown in Figure 12, which correspond to the earthquake locations for the three groups in Figure 7. Each group includes three events at the same depth to sample the area by the ray paths. The theoretical travel times of the P-wave first arrivals are 25.3, 26.6, and 27.9 sec for the epicentral distances at 160, 170, and 180 km for group A; 19.3, 20.9, and 22.4 sec for the epicentral distances at 110, 120, and 130 km for group B; and 9.9, 11.4, and 12.8 sec for the epicentral distances at 50, 60, and 70 km for group C, respectively. Compared to the observed travel times at station SL21 in Figure 4b, the observed travel times for groups A, B, and C are of about 26–28, 17–20, and 10–12 sec, respectively. In general, the observed and theoretical travel times are similar. Therefore, we can use the ray paths to locate the probable depth of the low-Q zone. Regarding the multipaths of P waves for an event, differences in theoretical travel times are less than 2 sec, which would be included in the signal time window for estimation of the amplitude spectrum. According to the observed t^*, the ray paths from group B are most likely to pass through the anomalous zone. Specifically, the zone through which the rays from group B pass but the rays from groups A and C do not pass will be the most probable location

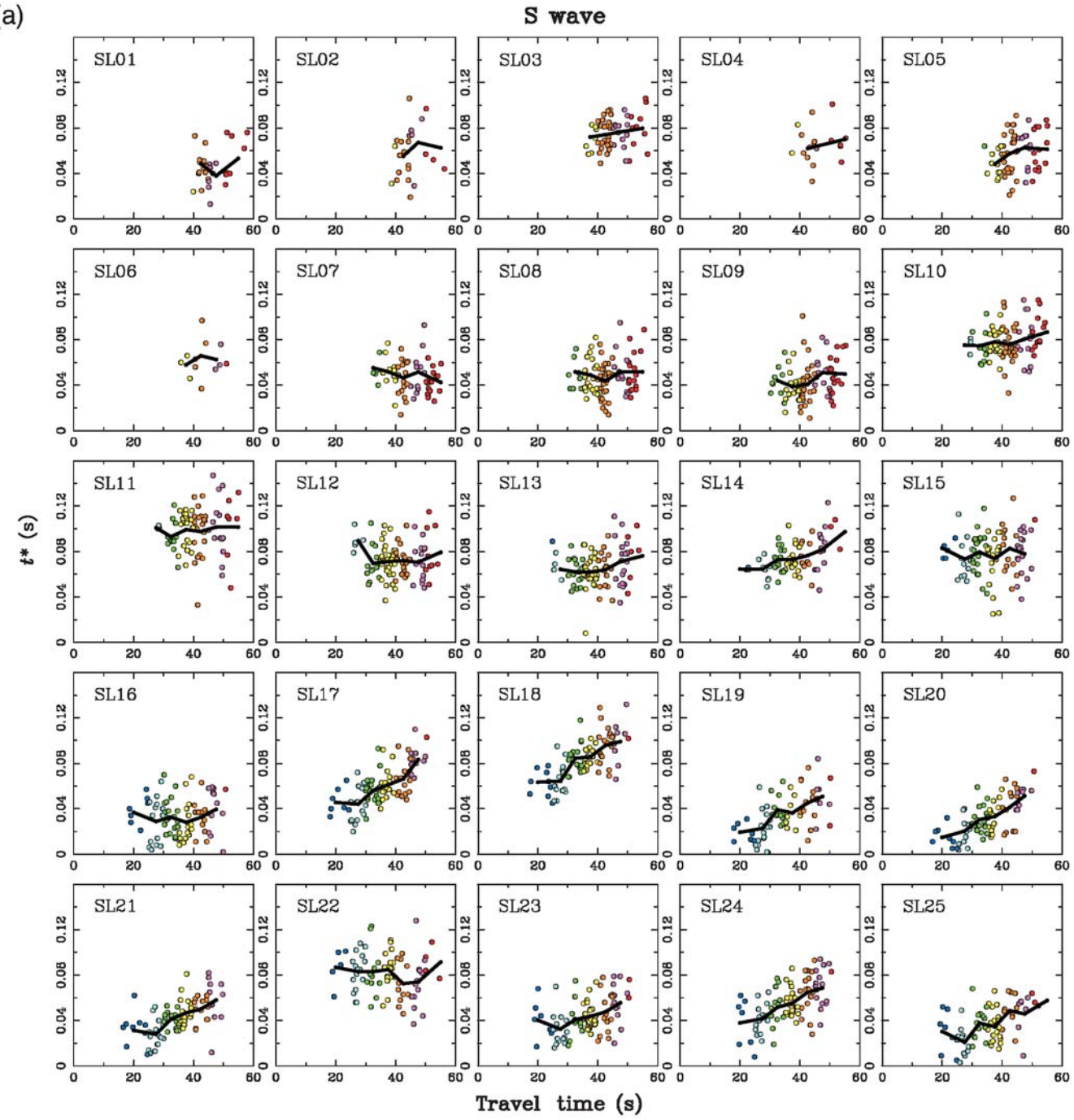

Figure 8. Plots of t^* versus travel time for an *S* wave. (a) t^* data excluding group B events with a depth shallower than 12 km. (b) t^* data only from group B events with a depth shallower than 12 km. The black line shows the average of t^* at 5 sec intervals. The colored dots denote increasing travel time from blue to red. (*Continued*)

of the anomalous zone. Our results suggest a probable depth at about 15–20 km.

Discussion

Our results show considerable scattering of t^* with reference to the best-fitting theoretical spectrums for individual stations. This scattering may be due partly to uncertainties in t^* estimations due to data quality, source location, and the model for source spectrum, and partly due to actual complex structures including path and site parts of attenuation. These factors are discussed subsequently.

The uncertainties in t^* estimations due to data quality are considered to be minimal because high-quality broadband seismic data are selected and processed with stringent criteria. However, because t^* is assumed independent of frequency,

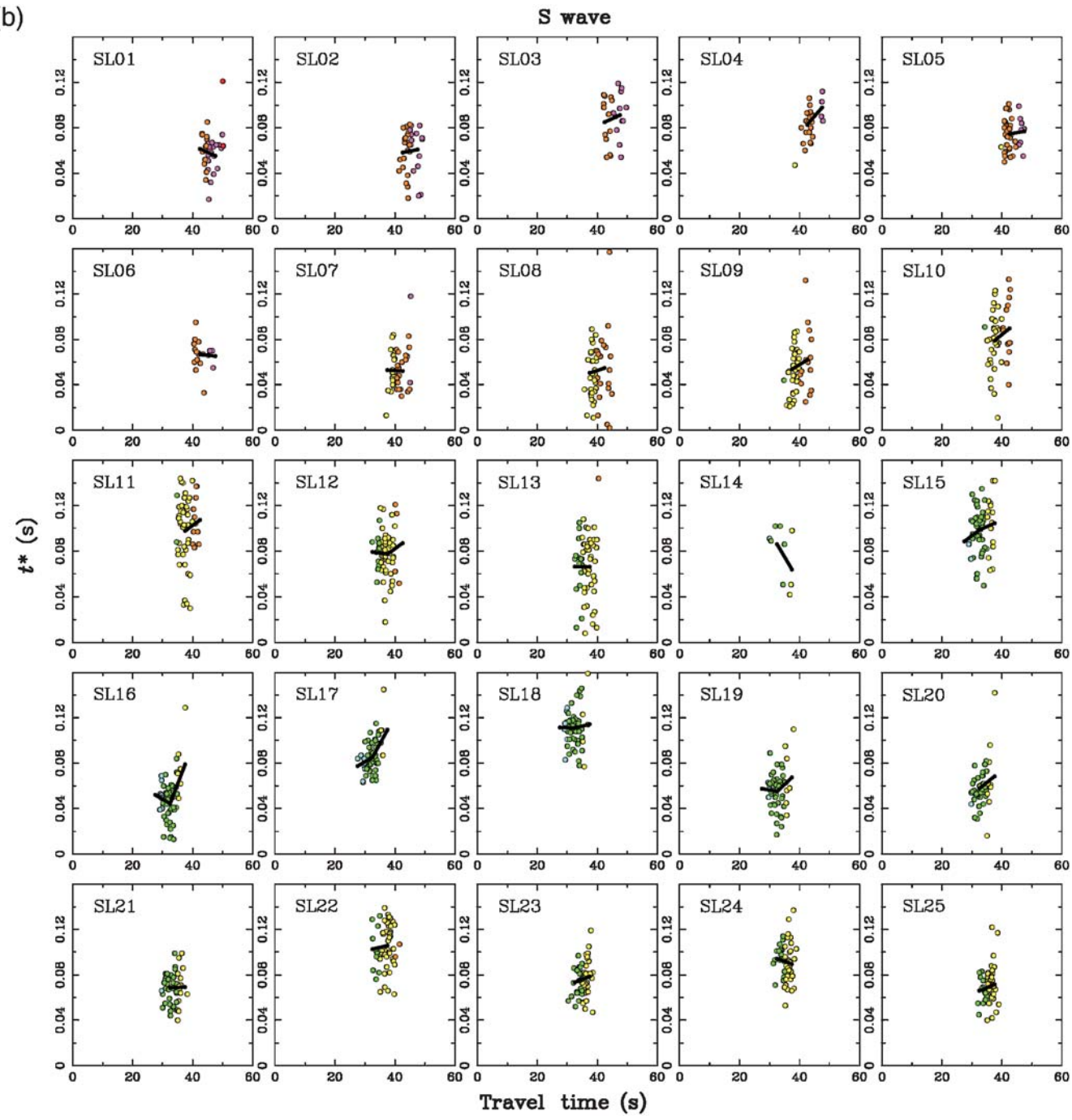

Figure 8. Continued.

the estimation of t^* will be affected if this is not the case in the real world.

Regarding the effect of the model for the seismic source spectrum, the corner frequency at all individual stations should be the same for a common event. Previous studies have shown that the difference between constrained and unconstrained f_c is not significant (Sarker and Abers, 1998). Therefore, f_c is not constrained in this study. Obviously, estimation of t^* can be affected by f_c because of trade-off effects (Schlotterbeck and Abers, 2001). Because the fitting of spectra for Ω_0 is not fixed at each station for a common event, the radiation pattern of the earthquake is included in the Ω_0. It is not necessary to consider the effect of the radiation pattern on individual stations at different azimuths. In addition, an ω^2 model for the source spectrum (Aki, 1967; Brune, 1970) is used as a reference to determine t^* from observations. Any deviation between the real source and the ω^2 model will affect the estimation of t^*.

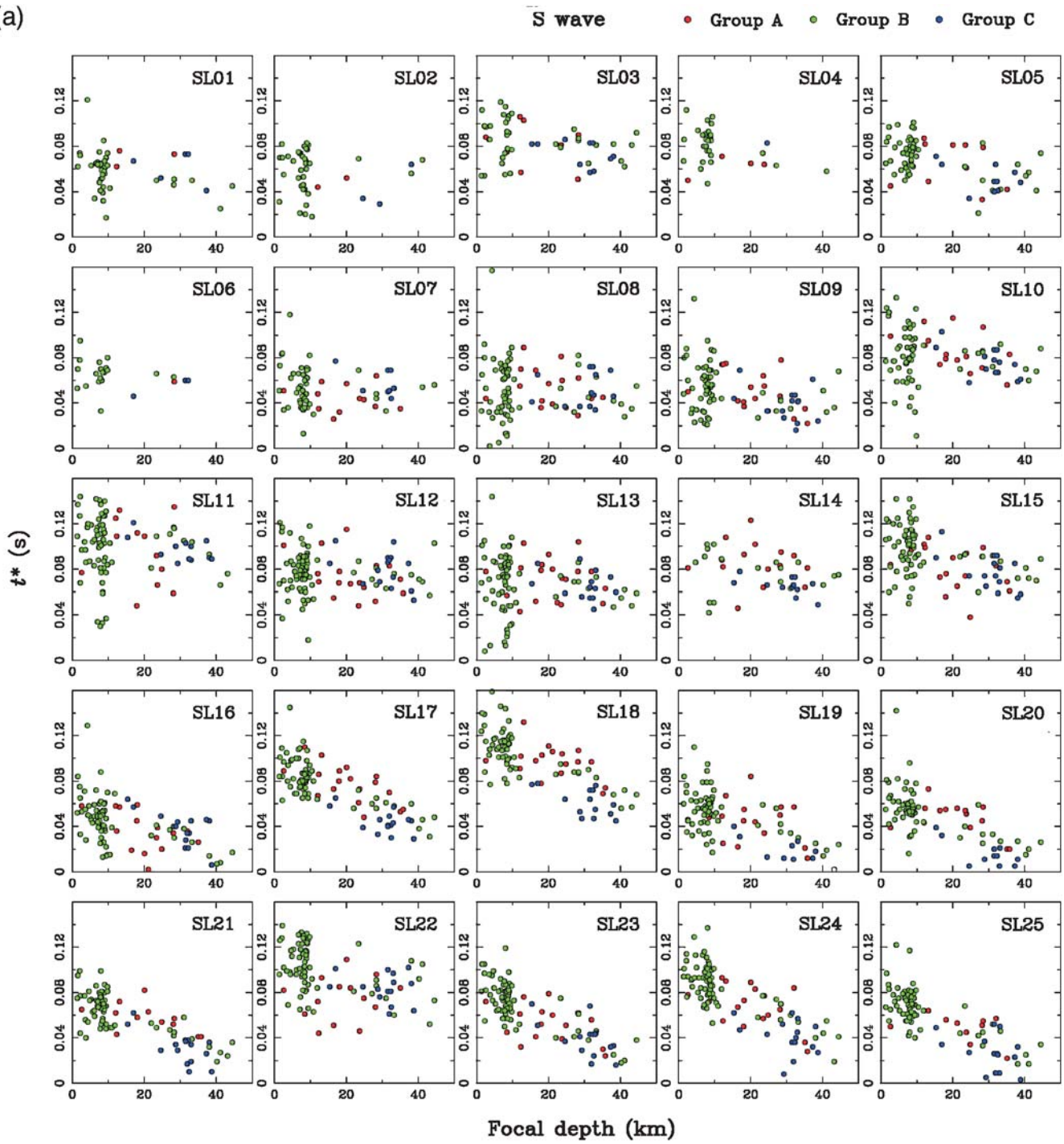

Figure 9. Plots of the t^* data versus focal depth for (a) *S* waves and (b) *P* waves. The three groups of events are denoted by different colors. The t^* decreases with focal depth for all groups. The t^* of groups A, B, and C gives high, medium, and low values, respectively, at the same focal depth for the eastern stations (SL17–SL25, except SL22). (*Continued*)

The uncertainty in location may be large if the events are far outside the network. However, most of our earthquakes are located along the coast or in the near-offshore areas. So the effect of network coverage should be minor. In addition, velocity model, available readings, reading accuracy of arrival time, and earthquake location method will also affect the accuracy of earthquake location. In this study we use earthquake locations of the TCWB catalog resulting from consistent location procedures to reduce parts of the uncertainties due to earthquake location, even though systematic bias from the routine earthquake location may exist. As a check, a subset of the 153 earthquake locations is compared with the results of their relocations by a three-dimensional relocation method (Wu *et al.*, 2008) and by the Double Difference earthquake

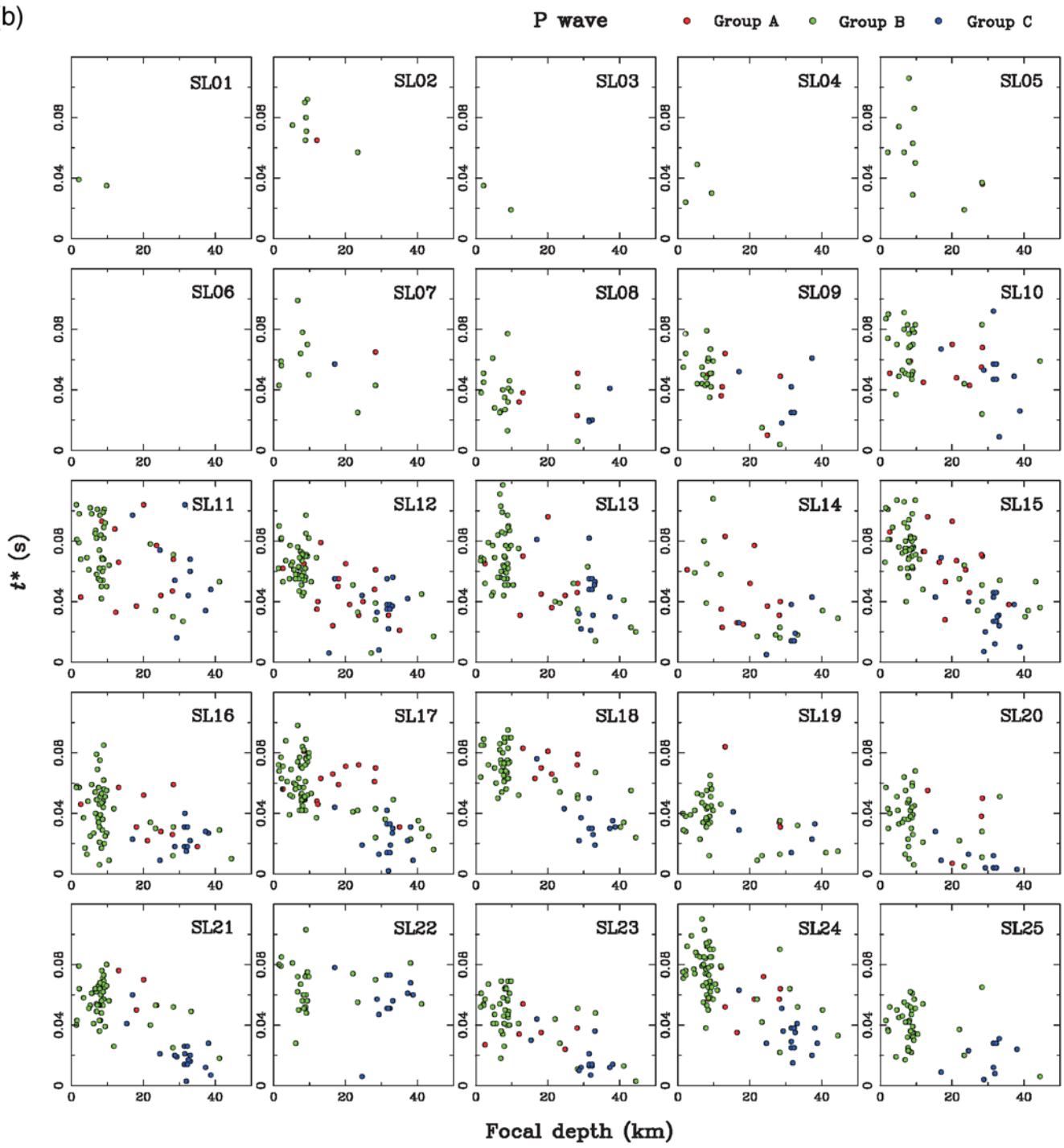

Figure 9. Continued.

relocation method using the hypoDD program (Waldhauser and Ellsworth, 2000) for the common events. These relocation results are not significantly different from the TCWB earthquake locations. The comparisons of results by different earthquake location methods show that the uncertainties due to earthquake location and origin time are minor for earthquakes on land or near the coast of Taiwan. The uncertainties are typically less than 2 km in epicenter, less than 5 km in focal depth, and less than 1 sec in origin time. This will minimally affect the t^* distribution in the plot of t^* with travel time. Furthermore, our method is relatively insensitive to the accuracy of earthquake location.

Regarding contamination of t^* for P and S waves due to complex structures, several factors may be involved. Scattering of the observed t^* may be due to path attenuation effects, including intrinsic and scattering attenuation, or due

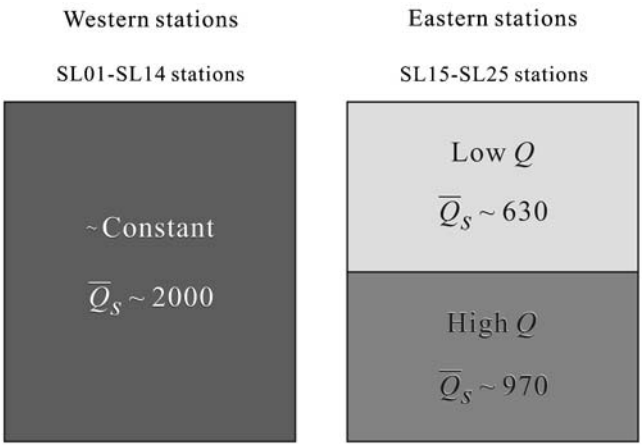

Figure 10. Schematic diagrams showing large contrast in crustal Q structures between the eastern (right) and western (left) stations. Significant variations of Q with depth are found along paths to the eastern stations whereas nearly constant Q structures are found along paths to the western stations. Approximate average Q_S values show the magnitudes of lateral and vertical variations in the crustal attenuation structures across southern Taiwan.

to focusing or defocusing effects (Bregman *et al.*, 1989). It is not easy to distinguish these factors in this study because we have used relatively long time windows that may include several phases. Liang *et al.* (2007) indicate that the crustal thickness along the suture zone in eastern Taiwan is thinner than in central and western Taiwan. This means that P_n will become the first arrival at the station east of the suture zone, which is faster than P_g by about 3–4 sec, whereas P_g should be the first arrival at the western stations. They might be sampling different structures, such as P_g for the crust and P_n for the upper mantle, due to different ray paths. Nevertheless, we are certain that P_g, rather than P_n, is the main phase analyzed in this study, noting that the amplitude

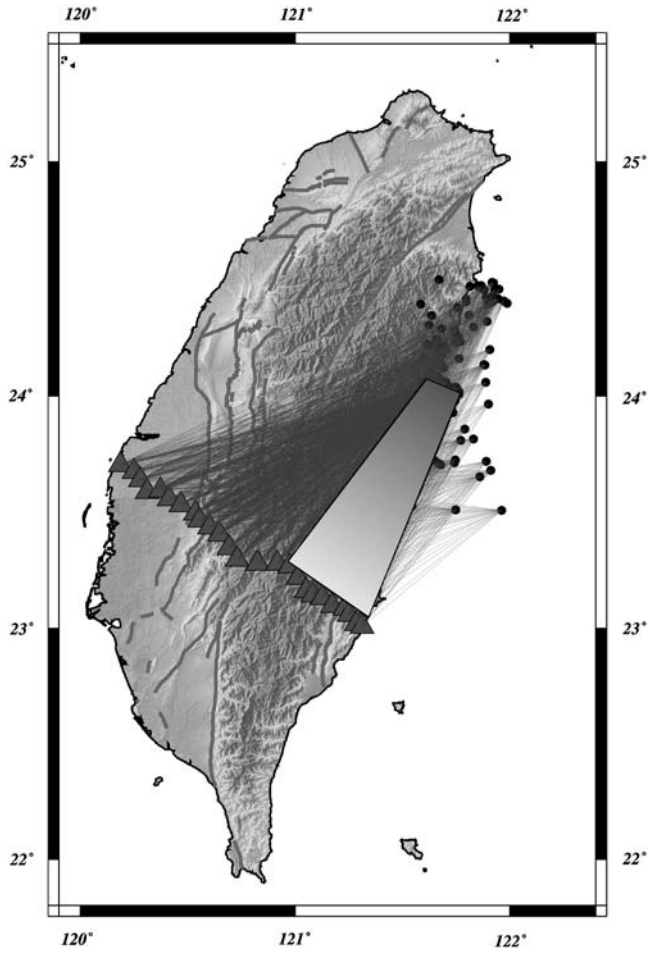

Figure 11. Probable area of high attenuation as delineated by this study is shown by the shaded zone. The triangles show seismic stations. The dots show the events. The thin lines show the ray paths of seismic waves. The thick lines show the active faults. The background shows the topography.

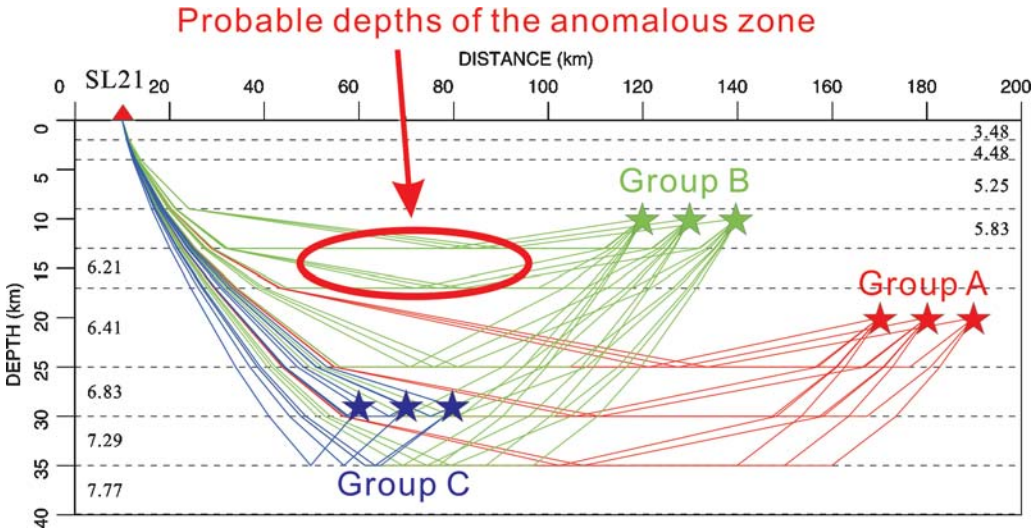

Figure 12. Ray paths from three groups of events are used to locate the probable depth of the high-attenuation zone. A one-dimensional P-wave velocity model is used. An eastern station (SL21) is depicted as an example.

spectrum is dominated by the phase with the largest energy that should be P_g, not the first arrival phase P_n, for the range of epicentral distances covered in this study (Lees and Lindley, 1994; Sarker and Abers, 1998). Besides, the time difference between P_n and P_g will be within the relatively long time window for our range of epicentral distances. Other phases may affect the t^* to cause scattering in t^*, but the uncertainty may be insignificant. Therefore, our analysis of seismic attenuation is focused on the crustal path effects.

Regarding the uncertainties from site effects, several factors may affect t^* estimation such as resonances in amplitude spectrum due to soil layers (Anderson and Hough, 1984) and background or cultural noise in some frequency band of the seismic signals. The influence will be limited because we use the frequency band from 1 to 20 Hz to estimate t^* in order to avoid the high-frequency noise problem.

Even though many factors may affect estimation of t^*, their influence will not be large enough to alter the results. Because the uncertainties of t^* estimation mentioned previously are negligible, we can use the results, which contain path and site effects, as shown in equation (4), to find complex attenuation structures. Regarding the site effects (t_0^*) on attenuation in t^*, t_0^* is included in t^* combining both path and site effects. The site effects on attenuation can be found empirically for each station from the data in Figure 4. Because all ray paths pass through the same shallow layers near a station, we can average all t^*s to obtain the characteristics of attenuation close to the station. Even though some path effects on attenuation may remain after averaging, the results can reveal trends of attenuation at each station due to site effects. Figure 13 shows the average and standard deviation of t^* at each station for S and P waves. From the figure we can find higher attenuation due to local site effects at SL11, SL15, SL18, and SL22 and lower attenuation at SL09, SL16, SL19, and SL20 for S waves. The difference in the average t^* at each station for S waves is larger than P waves. The patterns of the P waves are not always the same as the S waves. The peak and trough of average t^* are consistent at the stations to the east of SL08 for both P and S waves, but not for the stations to the west of SL08. It is interesting to note that the stations west of SL08 are located on alluvial plains where the S/N ratio is lower and the useful data are fewer than the stations east of SL08, especially for P waves. Besides, inconsistency of site effects on attenuation for P and S waves may be caused partly by different attenuation characteristics of P and S waves because the former is a compressional wave and the latter is a shear wave.

The site effect on attenuation, which cannot be ignored, plays an important role in controlling the amplitude of the seismogram. If not properly corrected, the results of fault rupture process inverted from observational seismograms may be severely affected. In addition, the amplification of waveforms will be overestimated by waveform simulations if anelastic behaviors of the path structures and local site conditions are not included. Thus, the site effect of attenuation is also important for assessment of earthquake hazards.

In summary, we can conclude that our results mainly represent the path effects on attenuation. The low-Q zone that we have identified is particularly significant. The probable location of the low-Q zone coincides with the aseismic zone (Figs. 1 and 11). It also overlaps with the low-P- and low-S-velocity zones (Ma *et al.*, 1996; Kim *et al.*, 2005). It was suggested that the low-velocity, aseismic zone may be

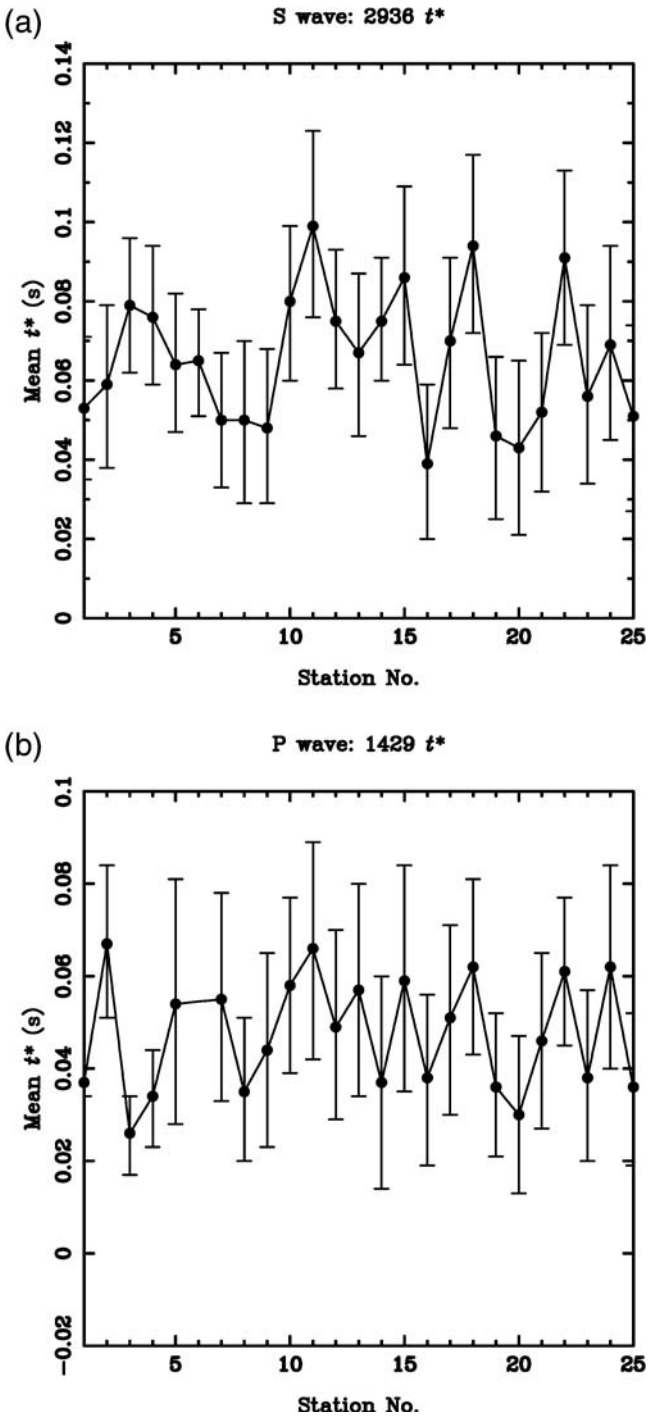

Figure 13. The range of t^* at individual stations for (a) S waves and (b) P waves. It shows the trend of site effects on seismic attenuation.

related to geothermal or partial melting effects (Ma *et al.*, 1996). Because high-underground temperature may result in greater dissipation of wave energy, the presence of a low-Q zone lends support to aforementioned interpretation. Furthermore, the lateral variations of seismic attenuation across southern Taiwan, which show relatively high attenuation in the east and relatively low attenuation in the west, are consistent with the observed heat flow patterns that show relatively high heat flows in the east and relatively low heat flows in the west (Lee and Cheng, 1986). Other geophysical results, including that of leveling (Liu and Yu, 1990), GPS (Yu *et al.*, 1997), and thermal modeling (Lin, 2000), also indicate that this particular area is directly related to the collision of the Philippine Sea and Eurasian plates.

Finally, our results on the observed attenuation parameter t^* in the collision boundary in Taiwan may be compared with other similar regions in the world. Attenuation structures in the boundary of the Alpine–Himalayan collision were studied by Sarker and Aber (1998). Their results indicated a significant discontinuity of attenuation between the platform and mountain areas. The average Q_S from linear regression of t^* versus distance is about 775 for the mountain areas, which is 2–3 times lower than average Q_S of about 2060 for the adjacent shields in Greater Caucasus. In this study the crustal average Q_S of 630–970 is estimated for the eastern Central Range of Taiwan, which is also 2–3 times lower than the average Q_S of about 2000 for western stations. Thus, the observed low-Q zone along the collision boundary in southeastern Taiwan is believed to be credible.

Conclusions

High-quality broadband seismic data of a dense linear seismic array across southern Taiwan were used to study the crustal attenuation structures. The parameters (Ω_0, f_c, and t^*) were obtained by fitting the seismic spectra. We took advantage of the geometry of the linear array to delineate spatial variations of t^* that in turn reveal both the lateral and depth variations of attenuation. Spatial variations of t^* were examined in terms of travel time, back azimuth, and focal depth. Lateral variations of attenuation along the linear array showed that attenuation over the eastern part of the array is significantly higher than the western part. The results were further combined to locate an anomalous zone of high-seismic attenuation for both P and S waves under the Central Range in southeastern Taiwan. Its depth is at about 15–20 km as judged from two-dimensional raytracing. The zone is under an area that is known to be aseismic with low-P and low-S velocities. The zone is probably caused by active geothermal or partial melting processes in the intense collision boundary of the Eurasian and Philippine Sea plates.

Data and Resources

Seismograms used in this study were collected by the Institute of Earth Sciences, Academia Sinica, Taiwan, and will be released to the public after the project is completed. The earthquake catalog is from the Taiwan Central Weather Bureau. Some plots were made using the Generic Mapping Tools version 4.2.1 (www.soest.hawaii.edu/gmt, last accessed October 2007; Wessel and Smith, 1998). Signal processing was done with Seismic Analysis Code (Goldstein *et al.*, 2003).

Acknowledgments

We would like to express our appreciation to the technical assistants at the Institute of Earth Sciences, Academia Sinica, who collected the seismic data. We also thank Colin Zelt and Uri S. ten Brink for providing the Ray-GUI program. The first author would like to thank the Earthquake Research Institute, University of Tokyo, for its support of the study during his visit there. Jer-Ming Chiu and another anonymous reviewer provided constructive comments and helpful suggestions to improve the article. Fruitful discussions with A. Kato, E. Kurashimo, and T. Iidaka at the Earthquake Research Institute, University of Tokyo, and C. H. Lin at the Institute of Earth Sciences, Academia Sinica, are appreciated. For this study, we used the computer systems of the Earthquake Information Center of the Earthquake Research Institute, University of Tokyo. This research was supported by the Institute of Earth Sciences, Academia Sinica, with contribution number IESAS1339 and the Taiwan Earthquake Research Center (TEC) funded through National Science Council (NSC) with Grant Number NSC97-2119-M-001-010. The TEC contribution number for this article is 00054.

References

Aki, K. (1967). Scaling law of seismic spectrum, *J. Geophys. Res.* **72,** 1217–1231.

Anderson, J. G., and S. E. Hough (1984). A model for the shape of the Fourier amplitude spectrum of acceleration at high frequencies, *Bull. Seismol. Soc. Am.* **74,** 1969–1993.

Bregman, N. D., C. H. Chapman, and R. C. Bailey (1989). Travel time and amplitude analysis in seismic tomography, *J. Geophys. Res.* **94,** 7577–7587.

Brune, J. N. (1970). Tectonic stress and the spectra of seismic shear waves from earthquakes, *J. Geophys. Res.* **75,** 4997–5009.

Brune, J. N. (1971). Correction: Tectonic stress and the spectra of seismic shear waves from earthquakes, *J. Geophys. Res.* **76,** 5002.

Chen, K. J. (1998). *S*-wave attenuation structure in the Taiwan area and its correlation to seismicity, *TAO* **9,** 97–118.

Chen, Y. L., and T. C. Shin (1998). Study of the earthquake location of 3-D velocity structure in Taiwan area, *Meteor. Bull.* **42,** 135–169.

Chen, K. J., Y. H. Yeh, and C. T. Shyu (1996). Q_P structure in the Taiwan area and its correlation to seismocity, *TAO* **7,** 409–429.

Eberhart-Phillips, D., and M. Chadwick (2002). Three-dimensional attenuation model of the shallow Hikurangi subduction zone in the Raukumara peninsula, New Zealand, *J. Geophys. Res.* **107,** no. B2, 2033, doi 10.1029/2000JB000046.

Goldstein, P., D. Dodge, M. Firpo, and L. Miner (2003). SAC2000: Signal processing and analysis tools for seismologists and engineers, in *International Handbook of Earthquake and Engineering Seismology*, W. H. K. Lee, H. Kanamori, P. C. Jennings, and C. Kisslinger (Editors), Vol. **81B**, Academic Press, London, 1613–1614.

Hough, S. E., J. G. Anderson, J. Brune, F. Vernon III, J. Berger, J. Fletcher, L. Haar, T. Hanks, and L. Baker (1988). Attenuation near Anza, California, *Bull. Seismol. Soc. Am.* **78,** 672–691.

Huang, B.-S., W.-G. Huang, W.-T. Liang, R.-J. Rau, and N. Hirata (2006). Anisotropy beneath an active collision orogen of Taiwan: Results from across islands array observations, *Geophys. Res. Lett.* **33,** L24302, doi 10.1029/2006GL027844.

Jones, T., and A. Nur (1983). Velocity and attenuation in sandstone at elevated temperatures and pressures, *Geophys. Res. Lett.* **10,** 140–143.

Kim, K. H., J. M. Chiu, J. Pujol, K. C. Chen, B. S. Huang, Y. Yeh, and P. Shen (2005). Three-dimensional V_P and V_S structural models associated with the active subduction and collision tectonics in the Taiwan region, *Geophys. J. Int.* **162,** 204–220.

Lee, C. R., and W. T. Cheng (1986). Preliminary heat flow measurements in Taiwan, Presented at the *4th Circum-Pacific Energy and Mineral Resources Conf.*, Singapore, 17–22 August 1986.

Lee, C. P., Y. B. Tsai, and K. L. Wen (2006). Analysis of nonlinear site response using LSST downhole accelerometer array data, *Soil Dyn. Earthq. Eng.* **26,** 435–460, doi 10.1016/j.soildyn.2005.10.005.

Lees, J. M., and G. T. Lindley (1994). Three-dimensional attenuation tomography at Loma Prieta: Inversion of t^* for Q, *J. Geophys. Res.* **99,** no. B4, 6843–6863.

Liang, W. T., J. M. Chiu, and K. Kim (2007). Anomalous *Pn* wave observed in eastern Taiwan: Implications of a thin crust and elevated oceanic upper mantle beneath the active collision-zone suture, *Bull. Seismol. Soc. Am.* **97,** 1370–1377, doi 10.1785/0120060226.

Lin, C. H. (2000). Thermal modeling of continental subduction and exhumation constrained by heat flow and seismicity in Taiwan, *Tectonophysics* **324,** 189–201.

Lindley, G. T., and R. J. Archuleta (1992). Earthquake source parameters and the frequency dependence of attenuation at Coalinga, Mammoth Lakes, and the Santa Cruz Mountains, California, *J. Geophys. Res.* **97,** no. B10, 14,137–14,154.

Liu, C. C., and S. B. Yu (1990). Vertical crustal movement in eastern Taiwan and its tectonic implication, *Tectonophysics* **183,** 111–119.

Ma, K. F., J. H. Wang, and D. Zhao (1996). Three-dimensional seismic velocity structure of the crust and uppermost mantle beneath Taiwan, *J. Phys. Earth* **44,** 85–105.

Sarker, G., and G. A. Abers (1998). Deep structures along the boundary of a collisional belt: Attenuation tomography of *P* and *S* waves in the Greater Caucasus, *Geophys. J. Int.* **133,** 326–340.

Scherbaum, F. (1990). Combined inversion for the three-dimensional Q structure and source parameters using microearthquake spectra, *J. Geophys. Res.* **95,** no. B8, 12,423–12,438.

Schlotterbeck, B. A., and G. A. Abers (2001). Three-dimensional attenuation variations in southern California, *J. Geophys. Res.* **106,** no. B12, 30,719–30,735.

Waldhauser, F., and W. L. Ellsworth (2000). A double-difference earthquake location algorithm: Method and application to the northern Hayward Fault, California, *Bull. Seismol. Soc. Am.* **90,** 1353–1368.

Wessel, P., and W. H. F. Smith (1998). New, improved version of the Generic Mapping Tools released, *Eos Trans. Am. Geophys. Union* **79,** 579.

Wu, Y. M., C. H. Chang, L. Zhao, T. L. Teng, and M. Nakamura (2008). A comprehensive relocation of earthquakes in Taiwan from 1990 to 2005, *Bull. Seismol. Soc. Am.* **98,** 1471–1481, doi 10.1785/0120070166.

Yu, S. B., H. Y. Chen, and L. C. Kuo (1997). Velocity field of GPS stations in Taiwan area, *Tectonophysics* **274,** 41–59.

Zelt, C. A., and R. B. Smith (1992). Seismic travel-time inversion for 2-D crustal velocity structure, *Geophys. J. Int.* **108,** 16–34.

Institute of Earth Sciences
Academia Sinica
Taipei, Taiwan
cplee@earth.sinica.edu.tw
(C.-P.L., N.H., B.-S.H., W.-G.H.)

Geosciences Department
Pacific Gas & Electronic Company
California
(Y.-B.T.)

Manuscript received 14 October 2008